Sustainable Structures
ISSN: 2789-3111 (Print); ISSN: 2789-312X (Online)
http://www.sustain-dpl.com/journal/sust
DOI: 10.54113/j.sust.2024.000039

ORIGINAL ARTICLE

Effects of aluminum alloy constitutive models on the behavior of concrete-filled aluminum tubular stub columns under axial compression

Jingxuan Wang[a,b], Jintao Zhao[a], Shan Gao[c,*], Anna Derlatka[d]

[a]School of Civil Engineering, Lanzhou University of Technology, Lanzhou, 730050, PR China.
[b]Western Center of Disaster Mitigation in Civil Engineering of Ministry of Education, Lanzhou University of Technology, Lanzhou 730050, PR China.
[c]School of Civil Engineering, Harbin Institute of Technology, Harbin 150090, China.
[d]Czestochowa University of Technology, Dabrowskiego 69, 42-201 Czestochowa, Poland.
[*]Corresponding Author: Shan Gao. Email: gaoshan@hit.edu.cn

Abstract: This study aims to examine the effects of various aluminum alloy constitutive models on the behavior of concrete-filled aluminum tubular stub columns under axial compression. The bi-linear model with hardening, the Baehre model, and the Ramberg-Osgood (R-O) model, which follow the European standard (EC9) were analyzed and compared in terms of their ability to describe the stress-strain behavior of aluminum alloy tensile coupons over the full range, and their respective application scenarios were discussed. A total of 74 sets of experimental data results were collected to examine the effects of these three models on the ultimate load of concrete-filled aluminum tubular stub columns. Furthermore, a full-scale model was constructed to analyze the effect of the hardening exponent *n* in the R-O model on the load-displacement curves. The results show that, apart from the bi-linear model with hardening, the other two aluminum alloy constitutive models are capable of accurately predicting the stress-strain behavior of aluminum alloys throughout the full range. The accuracy of the R-O model is significantly influenced by the calculation methods of *n*. The Baehre model is found to be more suitable for non-heat-treated aluminum alloys. The simulated ultimate load values obtained from the three constitutive models fall within a deviation range of ±10%, indicating their suitability for practical engineering applications. Among the three models, the R-O model exhibits the highest stability, as changes in the hardening exponent *n* do not affect the ultimate load but have a significant effect on the load-displacement curves beyond the ultimate load.

Keywords: Aluminum alloy constitutive models; concrete-filled aluminum tubular stub columns; axial compressive capacity; finite element analysis.

1 Introduction

Aluminum, the second largest category of metals, is the most extensively utilized metal variety following steel. Owing to its low density, it serves as a lightweight metal material primarily employed in the industry as an aluminum alloy. Aluminum alloy materials possess the characteristics of lightweight, aesthetically pleasing appearance, corrosion resistance, ease of maintenance, excellent durability, and low life cycle cost. They have extensive applications in the construction [1], packaging,

Received: 22 November 2023; Received in revised form: 12 April 2024; Accepted: 18 April 2024

electronics, and transportation sectors [2]. Among the various applications of aluminum alloys, its most familiar one is serving as a building decoration material, including aluminum alloy door and window frames, glass curtain wall support systems, and aluminum alloy exterior cladding of buildings.

Currently, various countries including China, the United States, Australia, and Europe have established design specifications for aluminum alloy structures. The code for design of aluminum structures (GB50429-2007) [3] in China stipulates that the elastic modulus of aluminum alloys is E = 70000 MPa (approximately 1/3 of that of ordinary steel), the Poisson's ratio is v = 0.3, and the yield strength of commonly used 6061-T6 series aluminum alloy tubes in construction is 240 MPa, with a tensile strength of 260 MPa. Aluminum alloy 6061 can achieve the strength of ordinary steel while exhibiting excellent corrosion resistance and low density (2700 kg/m^3), which is only about one-third that of steel. Initially employed predominantly as a building decoration material, aluminum alloy has subsequently evolved into integral structural components. Aluminum alloy structures, serving as load-bearing components, first emerged in Europe and America, encompassing aluminum alloy bridges, large-span roofs, grid shells, and trusses, as well as support systems for glass curtain walls. **Fig. 1** illustrates representative cases of domestic and international aluminum alloy structural engineering projects in recent years.

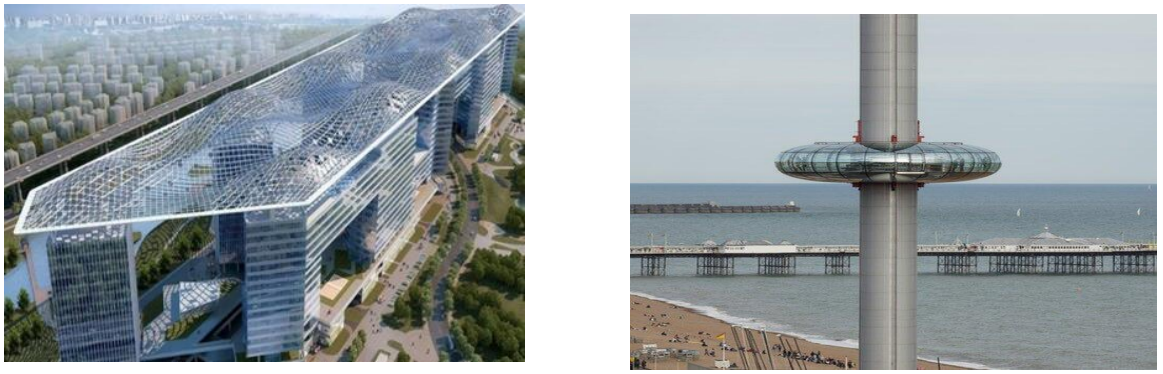

(a) Raphael Sky City (Shanghai, China, 2020) (b) i360 Mobile Sightseeing Tower (Brighton, UK, 2016)

Fig. 1. Recent typical aluminum alloy structure projects

In contrast to steel, the stress-strain curve of aluminum alloys lacks a distinct yield plateau and instead exhibits a continuous and smooth curve. The classical three-parameter Ramberg-Osgood model [4] (hereinafter referred to as the R-O model) has found extensive application in the mechanical analysis of aluminum alloy components [5-7]. However, the European standard EN 1999-1-1:2007 [8] (hereinafter referred to as EC9) introduces several other constitutive models in addition to the R-O model. Based on their types, all models can be categorized into piecewise models and continuous models. Furthermore, piecewise models can be subdivided into bi-linear and three-linear models, with further categorization possible based on the existence of a hardening stage. Continuous models can be categorized as the Baehre model [9] (expressed as σ=σ(ε)) and the R-O model (expressed as ε=ε(σ)) based on different expression forms. Previous studies [10-12] on aluminum alloy components have consistently emphasized the stability and buckling behavior of aluminum alloy columns, influenced by the lower elastic modulus of aluminum alloys. However, to counteract the propensity of aluminum alloy tubes to buckle, the concept of a concrete-filled steel tube can be employed, wherein the aluminum alloy tube is filled with concrete to fully exploit the mechanical properties of both materials. This combination of an aluminum alloy tube and concrete is referred to as concrete-filled aluminum alloy tubular (CFAT). In 2008 and 2009, Zhou and Young [13, 14] performed axial compression tests on rectangular and circular concrete-filled aluminum tubular (CFAT) stub columns, followed by numerical simulation studies [15] on circular CFAT stub columns in 2012. Zhou and Young [16, 17] proposed a formula for evaluating the load-bearing capacity of CFAT stub columns, which was subsequently validated in experiments, demonstrating the formula's high accuracy.

Over the past 15 years, there has been a significant number of extensive experimentations and numerical simulations conducted on CFAT columns featuring diverse cross-sectional geometries, encompassing circular [14, 18-26], rectangular (including square) [13, 27-30], circular double-skin [16,

31, 32], and other configurations involving double-tube composites [17, 33]. Due to the poor weldability of aluminum alloy tubes and the reduced strength caused by welding, the traditional eccentric loading method of welding the column and the end plate and connecting by placing the hinge is not suitable for CFAT columns, and a reasonable and reliable connection device needs to be set up. Therefore, there are only a few reports on the research of eccentrically loaded CFAT columns [34, 35]. At present, researchers generally use the R-O model and its modified version [36-39] as the constitutive model of aluminum alloy for CFAT stub columns, mainly because the model can produce results consistent with the actual behavior when simulating aluminum alloy structures. Based on the experience accumulated in the study of aluminum alloy structures, the researchers applied it to the study of such composite structures. But EC9 not only defines the R-O model as the only constitutive model for aluminum alloys. Compared with aluminum alloy components, there is a significant difference in the contribution of concrete and aluminum alloy to the bearing capacity under pressure, and the interface bonding force between the two materials will produce a significant combination effect so that it cannot be simply regarded as a direct superposition of material strength. Because of the complexity of numerical analysis caused by the above factors, it is necessary to conduct further investigations to ascertain whether employing alternative classical aluminum alloy constitutive models in simulating the composite columns can yield outcomes that align with those obtained using the R-O model.

To summarize, this study initiates from the practicality of aluminum alloy constitutive models and chooses three representative models: the bi-linear model with hardening, the Baehre model, and the R-O model, within the EC9. For testing purposes, a total of eight longitudinal tensile coupons, each with a thickness of 2.5mm, were extracted from both circular and square 6061-T6 aluminum tubes. By utilizing the existing tensile test data for aluminum alloys, a comprehensive comparison and evaluation of the descriptive characteristics and accuracy of these models in describing the stress-strain relationship of aluminum alloys were conducted. Moreover, explicit utilization scenarios of diverse constitutive models were thoroughly examined. The experimental data of 74 pieces of concrete-filled aluminum tubular (CFAT) stub columns were collected from home and abroad and analyzed numerically using ABAQUS software. Although numerous studies and discussions have focused on concrete constitutive models for CFAT stub columns under axial compression, there remains a dearth of research on aluminum alloy constitutive models for these components. The research conducted by Wang et al. [22] demonstrated the suitability of Han's concrete model [40] in simulating CFAT axial compression members. Consequently, Han's concrete model was employed for simulation purposes in this study. Subsequently, the ultimate load obtained from three distinct aluminum alloy constitutive models was computed, compared, and rigorously evaluated. Furthermore, the effect of the hardening exponent n in the R-O model on the load-displacement curve of CFAT stub columns under axial compression was quantitatively assessed. These endeavors facilitate a more extensive understanding of the variances among distinct aluminum alloy constitutive models, thereby furnishing an expanded array of dependable choices for the finite element analysis and engineering design of CFAT stub columns under axial compression.

2 Selection and comparison of typical constitutive models for aluminum alloys

2.1 Characteristics and preliminary evaluation of the selected models

Table 1 presents a comprehensive summary of the fundamental categories, indispensable parameters, applicable strain intervals, distinctive features, and initial assessment of the three chosen constitutive models examined in this investigation.

2.2 Bi-Linear Model with Hardening

Eq. (1) presents the expression of the bi-linear model with hardening, while **Fig. 2** illustrates its stress-strain relationship curve. The figure demonstrates that the bi-linear model with hardening fails to accurately depict the seamless transition of the stress-strain curve for the aluminum alloys from the elastic to the plastic stage. Moreover, the model anticipates the yield strain at the nominal yield point in advance, restricting the definition of the stress-strain relationship within a limited range of $0.5\varepsilon_u$ to avoid overestimating the strength within the strain hardening range.

$$\sigma = \begin{cases} E\varepsilon & 0 < \varepsilon \le \varepsilon_p \\ f_p + E_1(\varepsilon - \varepsilon_p) & \varepsilon_p < \varepsilon \le \varepsilon_{max} \end{cases} \quad (1)$$

where f_p is the conventional elastic limit of proportionality, ε_p, and ε_{max} correspond to the strain at f_p and f_{max}, E is the elastic modulus, E_1 is the hardening modulus. In the absence of a more accurate assessment of the aforementioned parameters, the following assumed values can be used: f_p = nominal value of $f_{0.2}$ ($f_{0.2}$ represents the conditional yield strength corresponding to residual strain of 0.002), f_{max} = nominal value of $f_{0.2}$, and ε_{max} = 0.5ε_u (ε_u denotes the nominal value of ultimate strain), ε_p = $f_{0.2}/E$, E_1 = (f_u-$f_{0.2}$)/(0.5ε_u-ε_p).

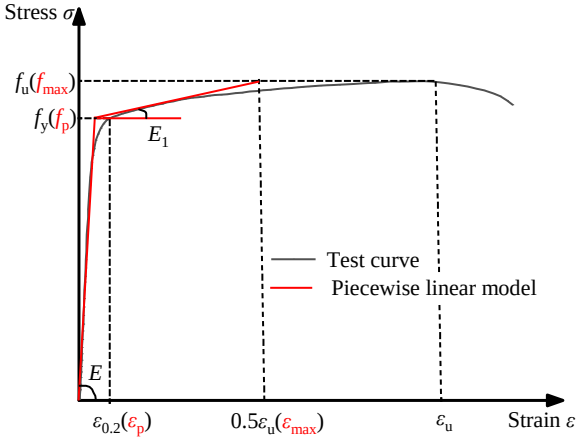

Fig. 2. Bi-linear model with hardening

Table 1. Three typical selected models

Models	Bi-linear model with hardening	Baehre model	R-O model
Type	Piecewise model ($\sigma = \sigma(\varepsilon)$)	Continuous model ($\sigma = \sigma(\varepsilon)$)	Continuous model ($\varepsilon = \varepsilon(\sigma)$)
Parameters required	$f_{0.2}$, E, ε_u, f_u	$f_{0.2}$, E, ε_u, f_u	$f_{0.2}$, E (Steinhardt simplification); $f_{0.1}$, E, $f_{0.2}$ (elasticity analysis); $f_{0.2}$, E, f_u (plasticity analysis)
Scope of application	$0 < \varepsilon \le 0.5\varepsilon_u$	$0 < \varepsilon \le 0.5\varepsilon_u$	$0 < \varepsilon \le \varepsilon_u$
Specificities	It cannot describe the nonlinear behavior of the σ-ε curve.	It can describe the nonlinear behavior of the σ-ε curve.	When the test curve is known, the model parameters can be determined by fitting experimental data or using empirical formulas.
Preliminary evaluation	A simple formula with a limited range of applications.	A complex formula with a limited range of applications.	A concise formula that subdivides various analytical conditions with a full range of applications.

2.3 Baehre Model

Eq. (2) presents the expression of the Baehre model, while **Fig. 3** illustrates its stress-strain relationship curve. The elastic behavior is represented by region 1, the inelastic behavior by region 2, and the strain-hardening behavior by region 3. Each region exhibits distinct stress-strain relationships that must maintain continuity at their respective limiting points. The stress-strain relationship defined by the Baehre model is limited to the range of 0.5ε_u. Within this range, it is bounded by $0.5\overline{\varepsilon_e}$ (ε_p) to

separate the elastic and inelastic behavior, and by $1.5\overline{\varepsilon_e}$ (ε_e) to distinguish the inelastic behavior from the strain-enhanced behavior.

$$\sigma=\begin{cases} E\varepsilon & 0<\varepsilon\le\varepsilon_p\left(\text{R1, elastic behavior}\right) \\ f_e\left[-0.2+1.85\dfrac{\varepsilon}{\varepsilon_e}-\left(\dfrac{\varepsilon}{\varepsilon_e}\right)^2+0.2\left(\dfrac{\varepsilon}{\varepsilon_e}\right)^3\right] & \varepsilon_p<\varepsilon\le1.5\overline{\varepsilon_e}\left(\text{R2, inelastic behavior}\right) \\ f_e\left[\dfrac{f_{max}}{f_e}-1.5\left(\dfrac{f_{max}}{f_e}-1\right)\dfrac{\overline{\varepsilon_e}}{\varepsilon}\right] & 1.5\overline{\varepsilon_e}<\varepsilon\le\varepsilon_{max}\left(\text{R3, strain-hardening behavior}\right) \end{cases} \tag{2}$$

where f_e is the conventional elastic limit, f_{max} is the tensile strength at the top point of the σ-ε curve, $\varepsilon_p=0.5\overline{\varepsilon_e}$, $\overline{\varepsilon_e}=f_e/E$.

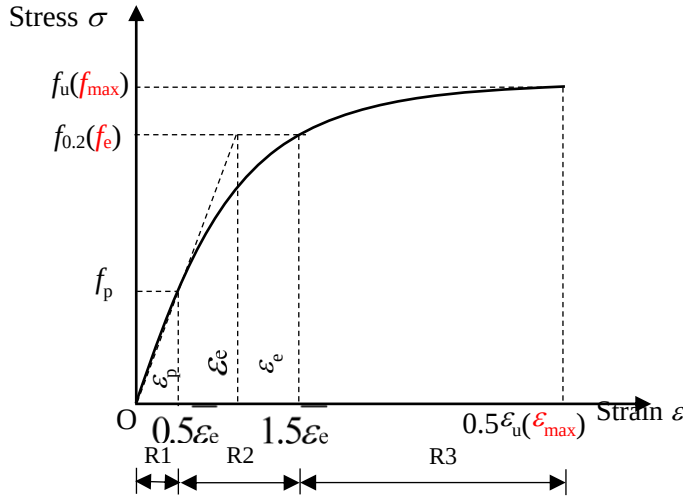

Fig. 3. Baehre model

2.4 R-O Model

Eq. (3) presents the expression of the R-O model, while **Fig. 4** illustrates its stress-strain relationship curve.

$$\varepsilon=\frac{\sigma}{E}+0.002\left(\frac{\sigma}{f_{0.2}}\right)^n,\ n=\frac{\ln\left(0.002/\varepsilon_{o,x}\right)}{\ln\left(f_{0.2}/f_x\right)} \tag{3}$$

where n denotes the exponent of the degree of hardening of the curve. To calculate the exponent n, it is necessary to know the second reference stress $f_{0.2}$, and its corresponding residual strain $\varepsilon_{o,x}$ in addition to the conditional yield strength $f_{0.2}$.

The selection of the second reference point ($\varepsilon_{o,x}$, f_x) should be based on the specific strain range relevant to the phenomenon being investigated. For analyses focusing on the elastic deformation range, the stress-strain obtained using the 0.1% offset method can serve as the second reference point (refer to **Fig. 4**(a)). In this scenario, $f_x=f_{0.1}$, $\varepsilon_{o,x}=0.001$, and n can be expressed in Eq. (4). Conversely, for analyses involving the plastic deformation range, the tensile stress at the top of the curve σ-ε can be regarded as the second reference point (refer to **Fig. 4**(b)). In such cases, $f_x=f_u$, $\varepsilon_{o,x}=\varepsilon_{u,pl}$, $\varepsilon_{u,pl}$ represent the residual strains corresponding to f_u, and n can be expressed in Eq. (5).

$$n_e=\frac{\ln 2}{\ln\left(f_{0.2}/f_{0.1}\right)} \tag{4}$$

$$n_{pl}=\frac{\ln\left(0.002/\varepsilon_{u,pl}\right)}{\ln\left(f_{0.2}/f_u\right)}\approx\frac{\ln\left(0.002/\varepsilon_u\right)}{\ln\left(f_{0.2}/f_u\right)} \tag{5}$$

where $\varepsilon_{u,pl}=\varepsilon_u-f_u/E$, and $\varepsilon_{u,pl}\approx\varepsilon_u$ since f_u/E is relatively small.

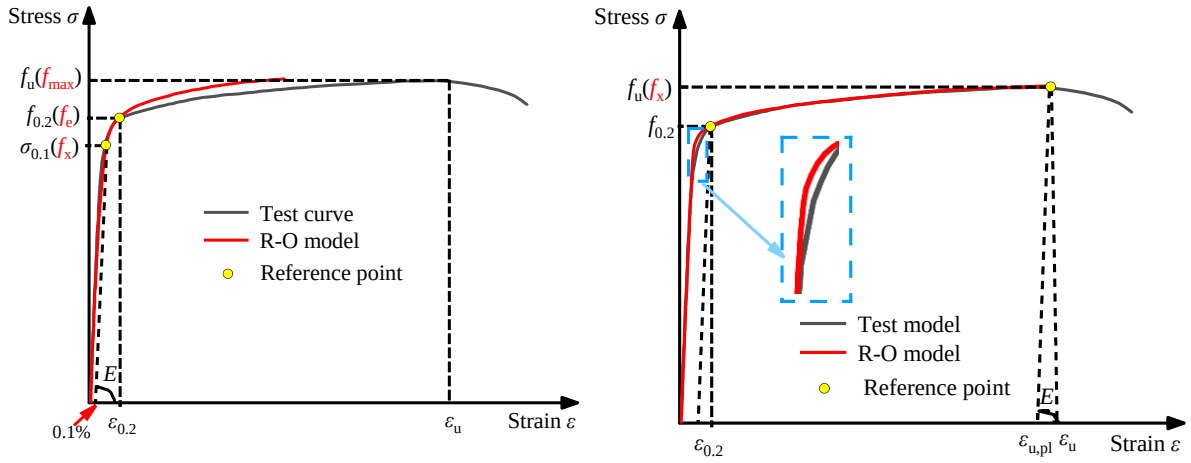

(a) Elastic deformation range (b) Plastic deformation range

Fig. 4. R-O model

Based on the equations provided above, the calculations of the value of n are complicated. Industry standards generally only provide E and $f_{0.2}$, making the application of the above model challenging. To address this issue, Steinhardt [41] proposed Eq. (6) in 1971, which has been widely tested and verified internationally. The value of $f_{0.1}$ can be determined by substituting Eq. (6) into Eq. (4).

$$10n=f_{0.2}\left(\text{MPa}\right) \tag{6}$$

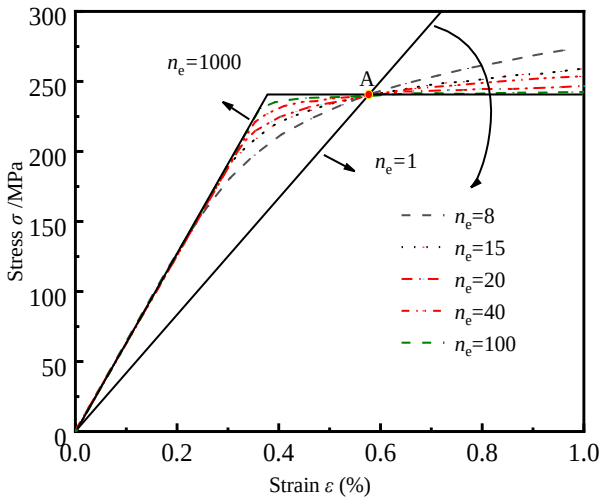

Fig. 5. Effect of n on R-O curves

Additionally, the value of n can be determined through fitting methods. It is a common engineering method to convert the R-O expression into a linear equation using double logarithmic coordinates and perform linear least squares fitting to determine its value. Wang et al. [42] proposed the utilization of the fast simulated annealing (FSA) algorithm to accurately determine the n value, which yields more stable results. Varying values of n_e alter the shape of the R-O model curve. For instance, consider using tubes from the 6061-T6 series specified in the GB50429-2007, which have material properties, such as E = 70,000 MPa, and $f_{0.2}$ = 240 MPa. As depicted in **Fig. 5**, every stress-strain curve intersects at point A $\left(\varepsilon_{0.2}+f_{0.2}/E,\ f_{0.2}\right)$, denoted as $\left(0.54\%,240\text{MPa}\right)$. When n_e = 1, the R-O model represents linear

elasticity, resulting in a straight line. For $n_e > 1$, the R-O model exhibits a continuously changing curve with a steeper "corner" as n_e increases. This indicates higher stress before point A and lower stress after point A, corresponding to a lower hardening modulus. When $n_e \rightarrow \infty$, the curve represents ideal elasticity, characterized by a bifold line without a hardening section.

2.5 Analysis of the Comparisons Between the Test Curves and the 3 Models' Predictions

An initial investigation was conducted to examine the constitutive relationship and mechanical properties of aluminum alloys via tensile coupon tests. Coupons were extracted from aluminum alloy 6061-T6 extruded tubes with circular or square cross-sections, each measuring 2.5mm in thickness. All coupons were longitudinally extracted from the aluminum alloy tubes, and their dimensions were processed by the specifications outlined in the GB/T 228.1−2010 [43]. The specific shape and dimensions are shown in **Fig. 6**.

Tensile tests were performed utilizing the SUNS electronic universal testing machine. During the tensile deformation, strain measurements were acquired using extensometers that matched the coupon gauge length specifications. The loading was carried out under room temperature conditions with a 0.2mm/min strain rate. **Fig. 7** displays the fractured coupons, revealing that the majority experienced fractures within the gauge length. Moreover, a more prominent necking phenomenon was observed at the fracture surface of coupons extracted from square tubes in comparison to those obtained from circular tubes.

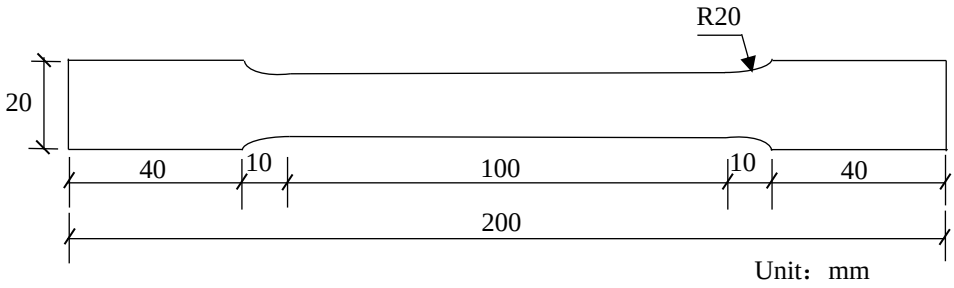

Fig. 6. Dimensions of tensile coupons

Fig. 7. Test setup and coupons after the tensile test

Table 2 displays key mechanical parameters obtained from tensile tests on aluminum alloys. **Fig. 8** illustrates comparisons between the stress-strain curves of the experimental measurements of the aluminum alloy tensile coupons and three selected models. Since the comparisons encompass the full curve range, the n of the R-O model is considered as n_{pl}. It is evident from **Table 2** that the n_e of the tensile coupons taken from circular tubes are relatively close to n_{pl}, whereas for square tubes, except for S-4, there is a notable disparity between n_e and n_{pl}. Therefore, the effect of the calculation methods of these two n values on the R-O model will be further examined in subsequent sections. Overall, among

the three selected models, the R-O model faithfully represents the stress-strain curves of the aluminum alloy tensile coupons. The bi-linear model with hardening initially slightly underpredicts the test curves within the range of $0.5\varepsilon_u$, but later reaches overall agreement. However, beyond the range of $0.5\varepsilon_u$, it increasingly deviates from the test curves, indicating that the bi-linear model with hardening cannot adequately simulate situations where large strains occur in aluminum alloys.

The Baehre model slightly overpredicts the strain-hardening behavior of aluminum alloy from the yield point to $0.5\varepsilon_u$, and then gradually approaches the test curves again after $0.5\varepsilon_u$, as shown in **Fig. 8** (e), (f), and (g). The strain hardening exponent n_e values are recorded for the respective tensile coupons as 71.37, 59.07, and 75.67. Considering **Fig. 5**, this suggests that these three tensile coupons exhibit relatively weak strain-hardening behavior, and the prediction deviation in their strain-hardening behavior is significantly larger than the other seven groups. Thus, it can be concluded that the Baehre model is not suitable for accurately predicting the strain-hardening behavior of aluminum alloys with low n_e values. Furthermore, based on the current predictions, the Baehre model demonstrates higher accuracy for predicting the stress-strain curves of aluminum alloys within n_e in the range of (1, 30]. Further discussions will be provided in the subsequent sections. Among the three constitutive models, only the Baehre model and the R-O model demonstrate the capability to accurately capture the characteristic roundedness of the stress-strain curves observed in tensile tests conducted on aluminum alloys. However, it is worth noting that the R-O model displays relatively higher accuracy in this regard, while the bi-linear model with hardening fails to capture the roundedness. Currently, none of the three constitutive models mentioned can predict the subsequent descending stage after a fracture occurs in the tensile coupons.

3 Discussion on the specific spplication scenarios of models

3.1 The effects of different calculation methods for the *n* on the R-O model curves

Table 2. Measured material properties obtained from tensile coupon tests

Specimen	$f_{0.1}$ (MPa)	$f_{0.2}$ (MPa)	f_u (MPa)	E_s (MPa)	v	ε_u (%)	$\varepsilon_{0.2}$	n_e	n_{pl}
C-1	242.8	246.7	268.7	71300	0.315	8.57	0.00546	43.50	43.99
C-2	230.2	233.0	251.9	64873	0.319	6.90	0.00559	57.33	45.40
C-3	235.4	240.6	261.7	72033	0.311	8.43	0.00534	31.72	44.51
C-4	230.3	234.8	257.7	68390	0.326	8.21	0.00543	35.82	39.92
Mean	234.7	238.8	260.0	69402	0.318	8.03	0.00546	40.02	43.41
S-1	174.2	175.9	221.1	66428	0.353	10.47	0.00465	71.37	17.30
S-2	177.9	180.0	224.1	66618	0.343	11.77	0.00470	59.07	18.60
S-3	195.6	197.4	244.0	73342	0.345	7.64	0.00469	75.67	17.19
S-4	218.8	221.2	236.7	62074	0.349	9.87	0.00551	63.54	57.57
Mean	191.6	193.6	231.5	68694	0.347	9.94	0.00489	66.75	21.85

Note: C indicates that this tensile coupon was taken from a circular tube, and S indicates that this tensile coupon was taken from a square tube. Here n_e is calculated according to Eq. (4) as the value of n considering elastic range analysis, and n_{pl} is calculated according to Eq. (5) as the value of n considering plastic range analysis.

Fig. 9 demonstrates the effects of two different calculation methods, Eq. (4) and Eq. (5), on the R-O curves. Specimens C-3, S-1, S-2, and S-3, which have the largest differences in calculated values of n, are selected to illustrate this discrepancy. As shown in **Fig. 8**, Eq. (4) is applicable to the range of elastic deformation. The R-O curves obtained with the calculated values n_e exhibit a higher degree of fit with the test curves before the yield point compared to the curves obtained with the calculated values n_{pl}, and they appear more complete before the yield point. However, after the yield point, the R-O curves using the calculated values n_e significantly deviate from the test curves, and their accuracy is lower than that of the R-O curves using the calculated values n_{pl}. When the test curves reach ε_u, the stress values corresponding to the R-O curves using the calculated values n_e are lower by 4.8%, 15.8%, 16.2%, and 20.3% compared to those using the calculated values n_{pl}. This observation indicates that although the R-O model is more accurate than the bi-linear model with hardening, it relies on selecting a reasonable calculation method for the n. If an appropriate calculation method for the n is not selected within the required analysis range, the accuracy of the R-O model may also be compromised.

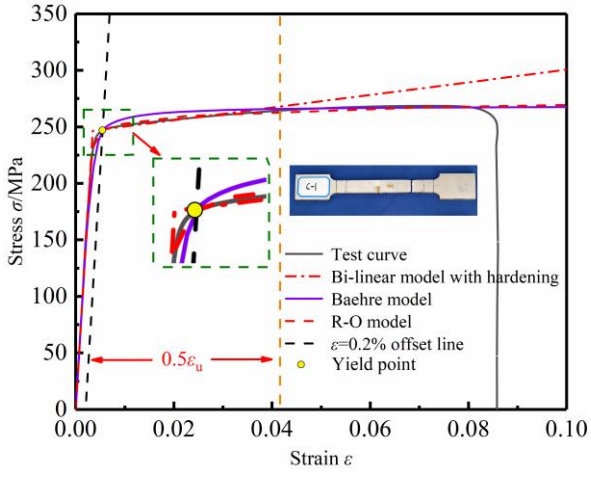

(a) C-1

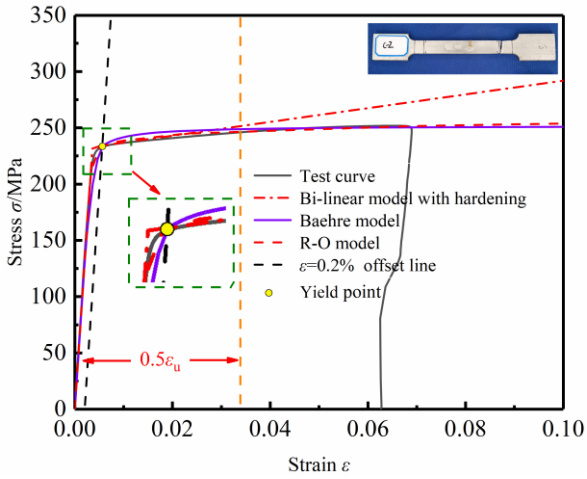

(b) C-2

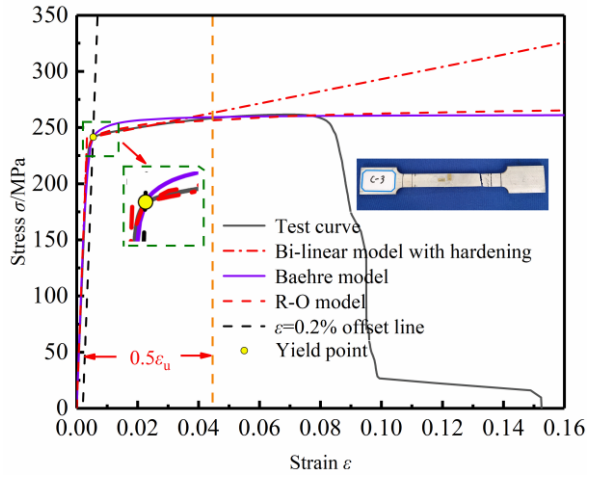

(c) C-3

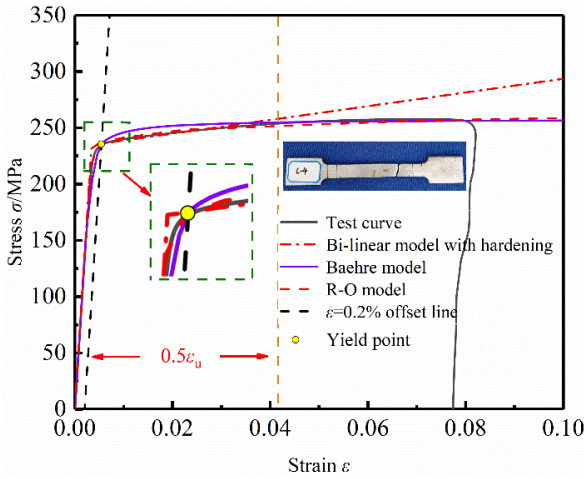

(d) C-4

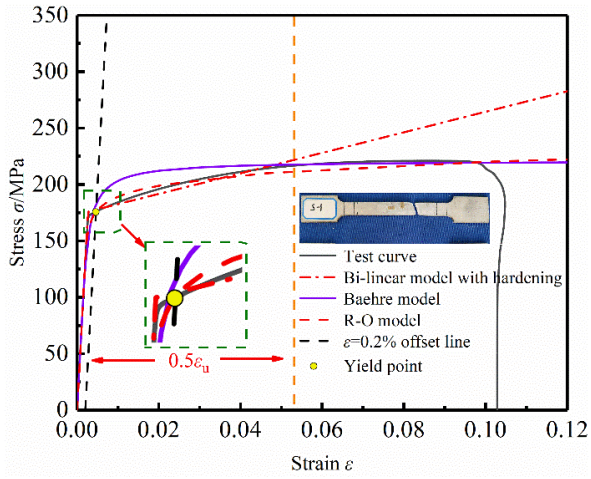

(e) S-1

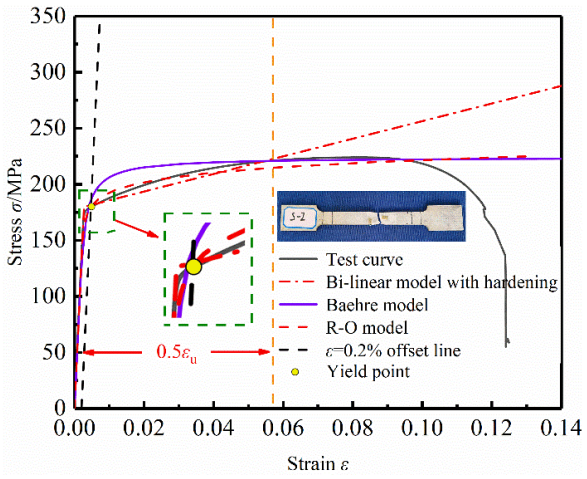

(f) S-2

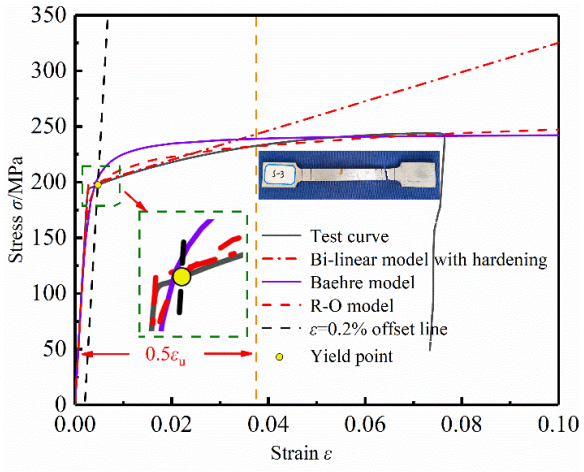

(g) S-3

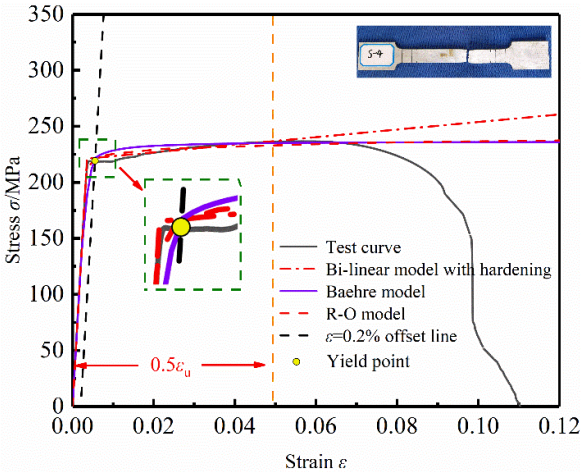

(h) S-4

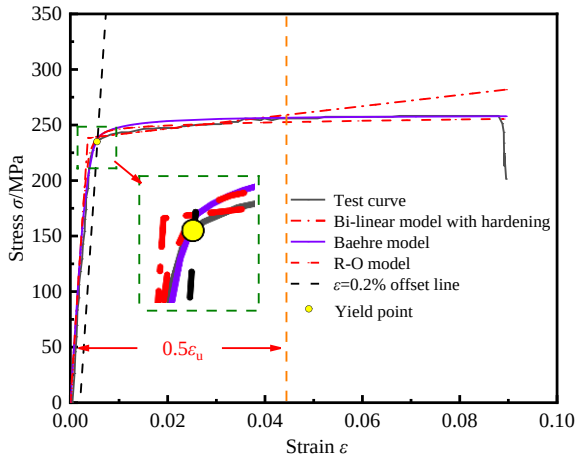

(i) CHS2 [14]

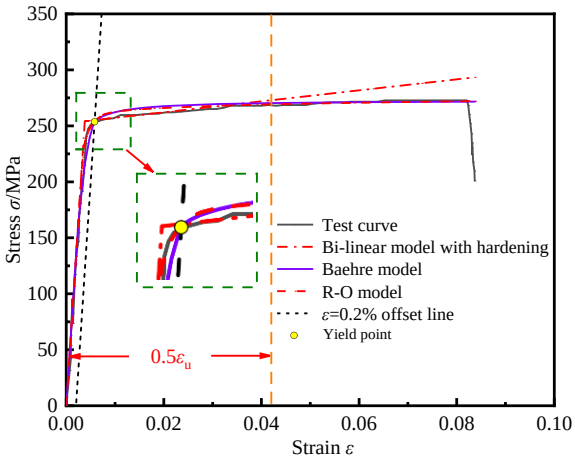

(j) CHS9 [14]

Fig. 8. Comparisons between the test curves and the 3 models' predictions

3.2 Exploration of the applicability of the Baehre model

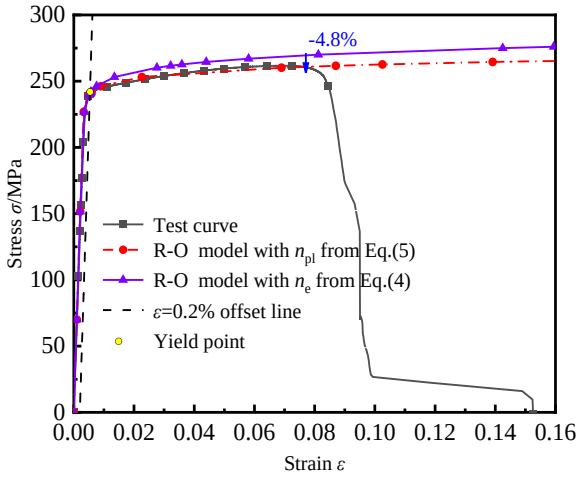

(a) C-3

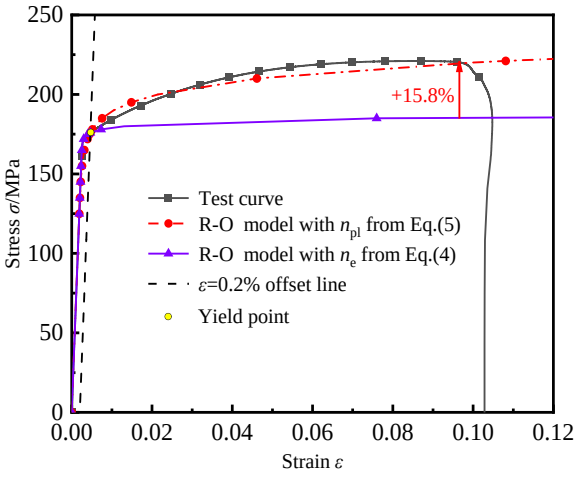

(b) S-1

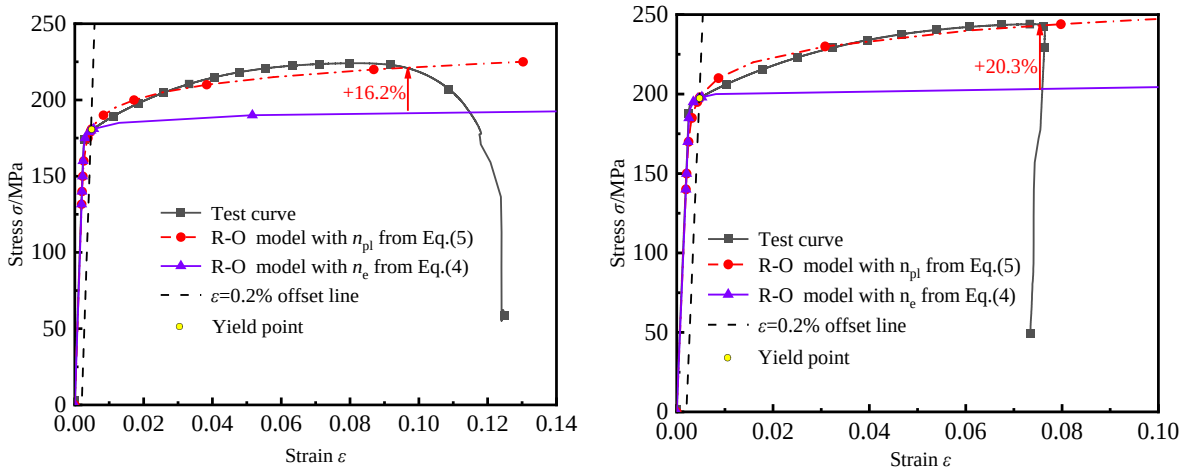

(c) S-2 (d) S-3

Fig. 9. Effects of different calculation methods for n values on R-O model curves

In section 2.5 of the comparative analysis, it can be reasonably inferred that the Baehre model demonstrates higher accuracy in predicting the stress-strain curve of aluminum alloys within n_e in the range of [1, 30]. Therefore, further investigation is conducted to explore the accuracy of the Baehre model within this specific range. Due to the limited availability of experimental data on tensile coupons within this range and the proven optimal accuracy of the R-O constitutive model, the typical R-O model curve of the 6061-T6 series aluminum alloy tubes in **Fig. 5** is considered to determine the range of n_e values that closely match the Baehre model curve. According to the GB50429-2007, ε_u is taken as 0.08 and f_u as 260MPa for the 6061-T6 tubes.

Fig. 10 illustrates that the Baehre model curve falls within the range of $8 < n_e < 15$, which corresponds to the R-O curve. For non-heat-treated aluminum alloys, the n_e values range from approximately 8 to 15, while for general heat-treated aluminum alloys, the n_e values range from approximately 20 to 40. Hence, it can be concluded that the Baehre model is more suitable for predicting the stress-strain curves of non-heat-treated aluminum alloys.

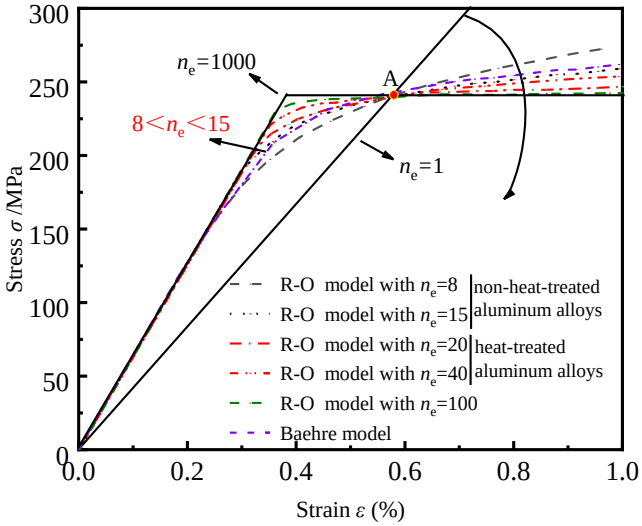

Fig. 10. Discussion of the Baehre model scope of application

4 Applicability assessment of three models for predicting the N_u of CFAT stub columns

4.1 Selection of simulated specimens for CFAT stub columns

The present study employs the bi-linear model with hardening, the Baehre model, and the R-O

model to conduct finite element simulations on CFAT stub columns under axial compression. The objective is to investigate the effects of these three models on the accuracy of the simulations. A total of 74 CFAT stub columns selected from [14, 16, 18, 19, 26, 32], are included in the analysis. The material parameters and geometric parameters of the CFAT stub columns are presented in **Fig. 11** and **Fig. 12** respectively.

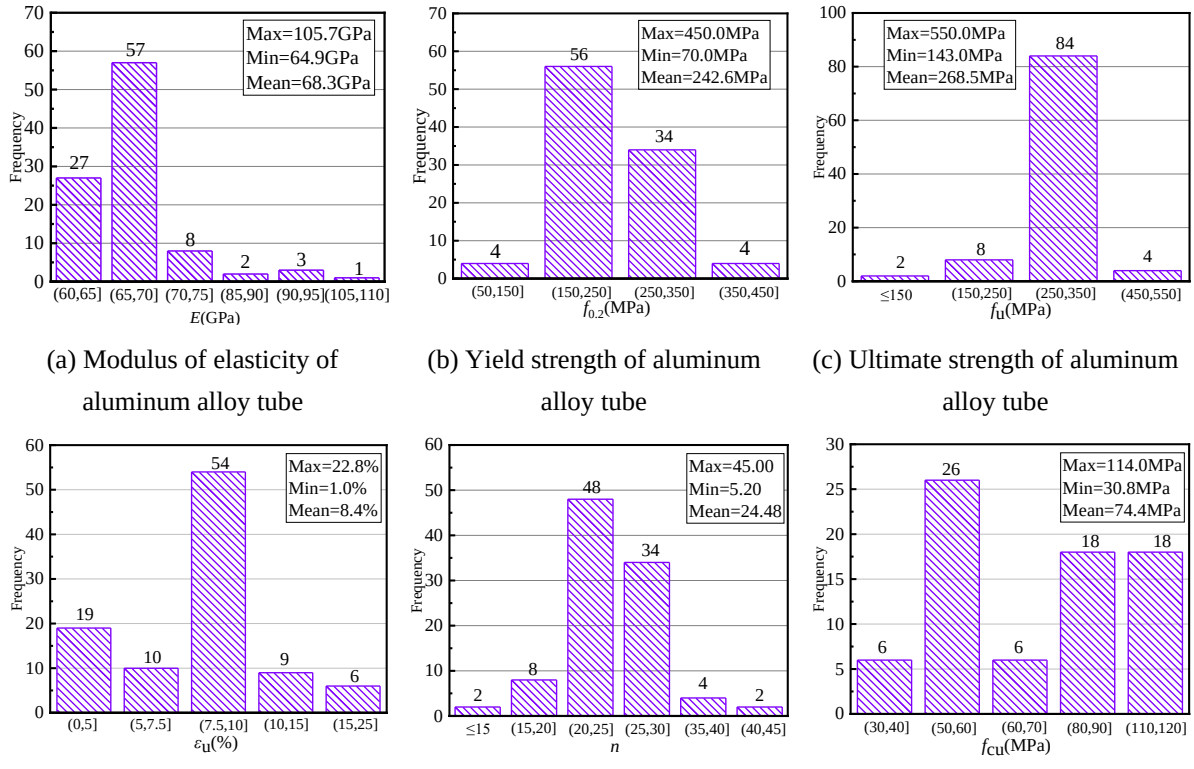

(a) Modulus of elasticity of aluminum alloy tube

(b) Yield strength of aluminum alloy tube

(c) Ultimate strength of aluminum alloy tube

(d) Ultimate strain of aluminum alloy tube

(e) Strain hardening exponent of aluminum alloy tube

(f) Compressive strength of concrete

Fig. 11. Material parameters of CFAT stub columns

From **Fig. 11**, it is evident that the material parameters primarily consist of the elastic modulus E, yield strength $f_{0.2}$, ultimate tensile strength f_u, ultimate strain ε_u, strain hardening exponent n of the aluminum alloy, as well as the compressive strength f_{cu} of concrete. The average elastic modulus of the aluminum alloy in the specimens measures 68.3 GPa, slightly below the standard value of 70 GPa. Aluminum alloy tubes with yield strength and ultimate tensile strength below 350 MPa constitute 95.9% of the total specimens, indicating a predominant focus on aluminum alloy tubes with standard strength levels in current research on CFAT stub columns. The average ultimate strain value for the aluminum alloy tubes in the specimens stands at 8.4%, signifying favorable ductility characteristics. The strain hardening exponent of the aluminum alloy tubes is a computed parameter. To facilitate calculations, this study employs Eq. (6) mentioned earlier, revealing that the strain hardening exponent n in this sample primarily ranges from 20 to 30.

The specimens encompass different types of concrete, including ordinary, high-strength, and ultra-high-strength concrete. Ordinary concrete accounts for 43.2%, while high-strength and ultra-high-strength concrete account for 32.4% and 24.4% respectively. To address the absence of standardized compressive strength values in the literature, this study utilizes the GB 50010-2015 [44] and formulas presented by Goode and Lam [45] to convert the prism strength f_c and cylinder strength of concrete to cube strength f_{cu}, as demonstrated in Eq. (7) and (8).

$$f_c=\alpha_1\alpha_2 f_{cu} \tag{7}$$

$$f'_c=0.8f_{cu} \tag{8}$$

where α_1 is the ratio of prismatic strength to cubic strength, and α_2 is the brittle discount factor for high-strength concrete, the exact values of which can be found in [44].

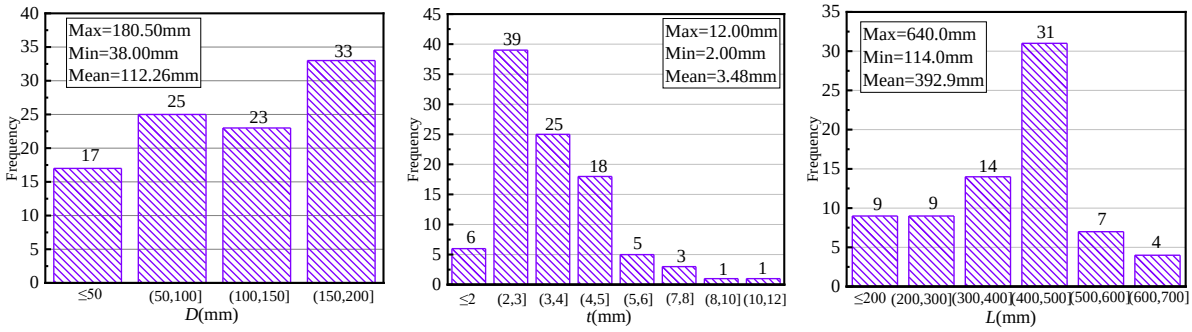

(a) Diameter of aluminum alloy tube (b) Thickness of aluminum alloy tube (c) Length of column

Fig. 12. Geometric parameters of CFAT stub columns

4.2 Modeling of simulated specimens and comparison of simulation results

The specimens' numerical models are established using the ABAQUS finite element software. Since simulation methods for such specimens are well-established, [15, 23] can be consulted for specifying element types, contact methods, and boundary conditions. Wang et al. [22] demonstrated that the constrained constitutive model proposed by Han [40] is suitable for simulating CFAT stub columns under axial compression. To ensure control over a single variable, the concrete constitutive model employed for the specimens in this study is Han's constitutive model. For specific details, refer to [40]. Three typical constitutive models for aluminum alloy were selected for simulating and comparing the ultimate load of CFAT stub columns. Refer to [46], Eq. (9) and (10) are utilized to transform the nominal stress-strain model into a true stress-strain model suitable for finite element simulation.

$$\sigma_{\text{true}}=\sigma_{\text{nom}}\left(1+\varepsilon_{\text{nom}}\right) \tag{9}$$

$$\varepsilon_{\text{ln}}^{\text{pl}}=\ln\left(1+\varepsilon_{\text{nom}}\right)-\sigma_{\text{true}}/E_0 \tag{10}$$

where σ_{true} and σ_{nom} are the true stress and nominal stress of the aluminum alloy respectively, $\varepsilon_{\text{ln}}^{\text{pl}}$ and ε_{nom} are the log plastic strain and nominal strain of the aluminum alloy respectively.

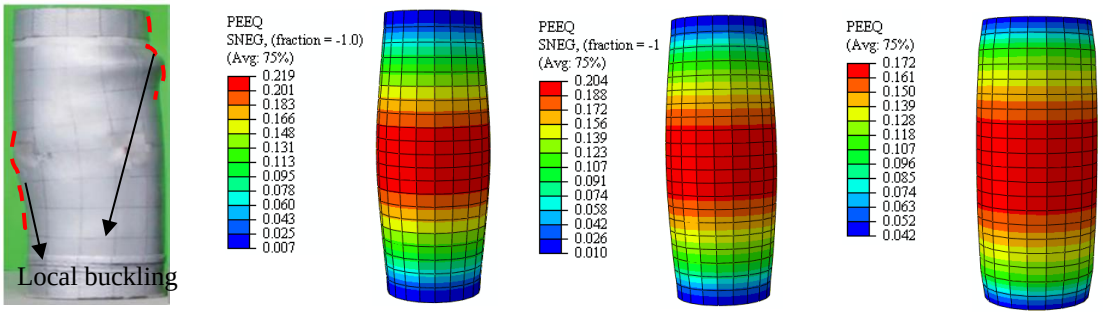

(a) Test failure mode [18] (b) Bi-linear model with hardening (c) Baehre model (d) R-O model

Fig. 13. Comparison of experimental and FE models

Fig. 13 shows the comparison of the experimental and FE analysis failure modes. The experimental specimens exhibited local buckling in the middle left and upper right, whereas the failure modes obtained from the three different aluminum alloy constitutive models all showed symmetrical local buckling only in the central region, still presenting a certain degree of discrepancy from the experimental failure modes. This is mainly because the finite element simulation was conducted under ideal conditions, whereas the axial loading in the experiment could not ensure eccentric-free loading. After all, all metal products are manufactured with permissible thickness deviations and the specimens themselves may have had initial defects. A comparison of the strain nephograms obtained using three

aluminum alloy constitutive models found that, except for the specimens using the R-O model, there was no significant deformation at the ends of the outer aluminum alloy tubes. However, the degree of deformation in the central part of the outer aluminum alloy tubes was as follows: the two-segment model exhibited the most significant deformation, followed by the Baehre model, with the R-O model showing the least deformation.

Fig. 14 and **Table 3** present a comparative analysis of the simulated ultimate load values obtained from three constitutive models and the corresponding experimental ultimate load values. The comparison reveals that the deviation in the simulated ultimate load values from the three constitutive models generally falls within a ±10% range. Both the Baehre model and the R-O model exhibit similar levels of simulation accuracy. However, the R-O model demonstrates greater stability in numerical simulations and lower variability compared to the Baehre model. Among the three constitutive models, the bi-linear model with hardening exhibits the poorest simulation accuracy and highest variability. Notably, extreme values may arise in the simulated values for large compressive strains in columns. Nevertheless, considering that the compressive strain limit state of columns in practical engineering scenarios does not reach such extreme experimental values, this model is still worth considering. **Table 3** indicates that only the simulated values obtained using the Baehre model exhibit slight conservatism. The average ratio of simulated values to experimental values is 0.998, with a coefficient of variation (COV) of 0.090. For the R-O model and bi-linear model with hardening, the average ratios of simulated values to experimental values are 1.009 and 1.040 respectively, with COV of 0.079 and 0.114. Thus, the simulated values obtained from these three constitutive models fall within an acceptable range for practical engineering applications.

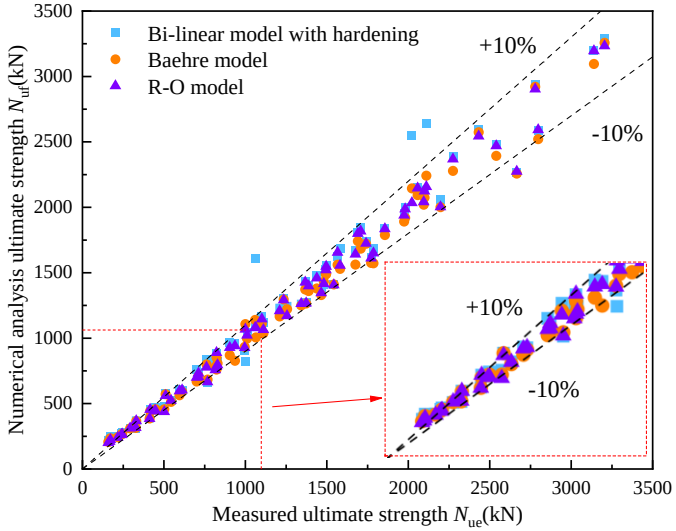

Fig. 14. Comparison of ultimate loads between measurements and numerical analysis

Table 3. Comparison of ultimate loads from simulation and test

Models	N_{uf}/ N_{ue}	Mean	COV
Bi-linear model with hardening	0.823~1.439	1.040	0.114
Baehre model	0.847~1.369	0.998	0.090
R-O model	0.853~1.265	1.009	0.079

4.3 The effects of n_e values on the N-Δ curves of CFAT stub columns

As mentioned in Section 3.1, the choice of different methods for calculating the value of n significantly affects the stress-strain curve of the R-O model. It is necessary to further discuss whether this effect will affect the load-displacement curve of the CFAT axial compression stub column model simulated using the R-O model. Additionally, **Fig. 12** demonstrates that all current experimental designs involve scaled specimens. Once the optimal R-O constitutive model is determined, this study refers to GB 50936-2014 [47] to establish the dimensions of the full-scale finite element model, using the following basic parameters: D=500mm, t=12mm, H=1500mm; f_{cu}=50MPa, $f_{0.2}$=240MPa. Varying

values of n are taken as 8, 24, 40, and 100.

Fig. 15(a) displays the R-O model curves for aluminum alloys with varying n_e values, while **Fig. 15**(b) illustrates the load-displacement curves of the CFAT axial compression stub columns with different n_e values. Assuming a synergistic behavior between the aluminum alloy tube and concrete under axial compressive loads, the strain of the aluminum tube at approximately 80 mm displacement of the CFAT stub column aligns with the dashed line in **Fig. 9**(a). This strain corresponds to four stress values, relative to the stress at n_e=100 during that instance. The stress values for n_e=8/24/40 exhibit increases of 43.7%, 10.2%, and 5.3% respectively. Likewise, at an 80mm displacement of the CFAT stub column, the load-displacement behavior, referring to the load at n_e=100, exhibits a corresponding pattern. The loads for n_e=8/24/40 demonstrate increases of 42.0%, 10.6%, and 4.8% respectively. This suggests that the substantial influence of various n_e values on the stress-strain curves of the R-O model can be transferred to the load-displacement curves of the CFAT axial compression stub column simulated with this model. The primary effect occurs after reaching the ultimate load but has minimal effect on the ultimate load itself.

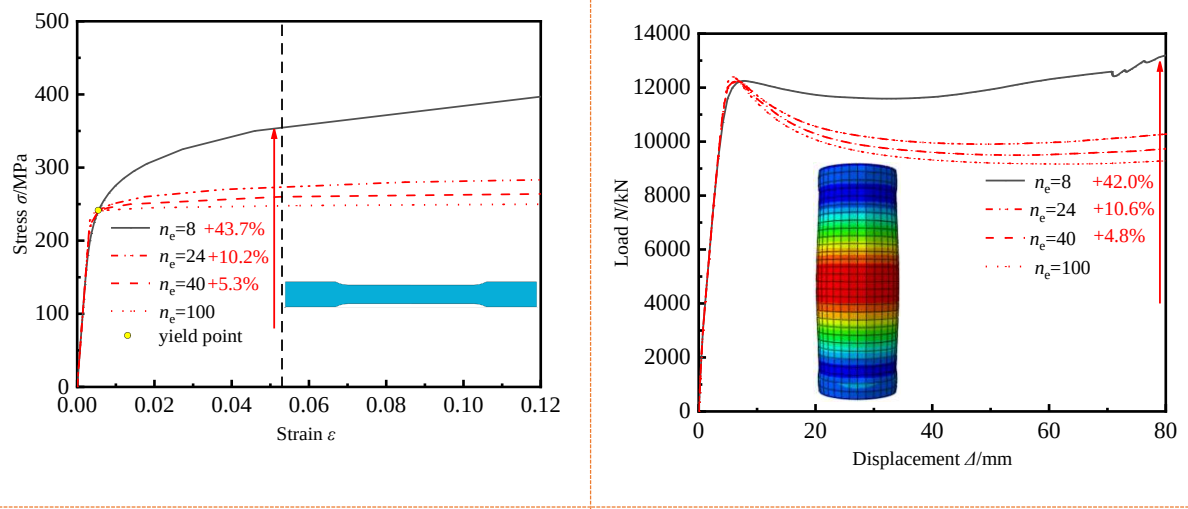

(a) R-O model curves of aluminum alloy tubes for different n_e

(b) Load-displacement curves of CFAT stub columns with different n_e

Fig. 15. Effects of strain hardening exponent

5 Conclusions

This paper explores three typical constitutive models for aluminum alloys and their capabilities in predicting stress-strain curves of tensile coupons, as well as their application scenarios. Moreover, the predictive effects and influential factors of these three models on the axial compressive load capacity of CFAT stub columns are studied. The following conclusions can be drawn:

(1) Only the R-O and Baehre models can accurately predict the full range of ultimate strain (ε_u). The bi-linear model with hardening is accurate only up to 0.5ε_u. The R-O model is the most accurate and can reliably represent the rounded stress-strain response typical of aluminum alloys, outperforming the Baehre model. In addition, since the typical aluminum alloy constitutive curves in this paper do not take fracture strain into account, they cannot predict the decline stage.

(2) The R-O model is found to be the most accurate and adaptable, with its curve shape adjusting to changes in the hardening exponent (n). There are various methods to calculate n, and the choice should be application-specific. The R-O model's accuracy heavily depends on the right n choice, with Steinhardt's formula being the simplest for this purpose.

(3) The Baehre model tends to overestimate the behavior in the strain-hardening phase, especially for alloys with limited strain-hardening capacity. As a result, it often produces fuller curves compared to the R-O model. The article suggests that the Baehre model's curve fits within the range of $8 < n_e < 15$ relative to the R-O curve, making it more suitable for predicting the stress-strain curves of unheated-treated aluminum alloys.

(4) For simulating the ultimate loads of CFAT stub columns under axial compression, the R-O model provides the most stable results, while the Baehre model is more conservative, and the bi-linear model with hardening is more prone to extreme values. For practical engineering, the simpler bi-linear model with hardening is recommended. When high accuracy is needed and stress-strain data from tensile tests are available, the R-O model is preferred.

(5) The effect of hardening exponent *n* on the R-O model affects the load-displacement curve of axially compressed CFAT stub columns, primarily influencing the descending stage after reaching the ultimate load but not affecting the ultimate load itself.

Acknowledgement

The authors would like to acknowledge the financially supported by the National Natural Science Foundation of China (No: 52368021, 52068047, 51908085), Lanzhou Youth Science and Technology Talent Innovation Project (No: 2023-QN-40) and Gansu Provincial Party Committee Organization Department talent (Longyuan Youth Innovation and Entrepreneurship talent) project.

CRediT authorship contribution statement

Jingxuan Wang: Conceptualization, Funding acquisition, Supervision, Investigation, Formal analysis, Writing – original draft. **Jintao Zhao**: Investigation, Formal analysis, Writing – original draft. **Shan Gao**: Supervision, Writing – review & editing. **Anna Derlatka**: Supervision, Writing – review & editing.

Conflicts of Interest

The authors declare that they have no conflicts of interest to report regarding the present study.

References

[1] Chybiński M, Polus Ł. Structural Behaviour of Aluminium–Timber Composite Beams with Partial Shear Connections. Applied Sciences, 2023; 13: 1603. https://doi.org/10.3390/app13031603.

[2] Szczucka-Lasota B, Węgrzyn T, Jurek A. Aluminum alloy welding in automotive industry. Transport Problems, 2020; 15: 67–78. https://doi.org/10.21307/TP-2020-034.

[3] GB 50429-2007. Code for design of aluminum structures. Ministry of Construction of the People's Republic of China, 2007. (In Chinese)

[4] Ramberg W, Osgood WR. Description of Stress-Strain Curves by Three Parameters. National Advisory Committee for Aeronautics, 1943; 902.

[5] Wang ZX, Wang YQ, Sojeong J, et al. Experimental investigation and parametric analysis on overall buckling behavior of large-section aluminium alloy columns under axial compression. Thin-walled structures, 2018; 122: 585-596. https://doi.org/10.1016/j.tws.2017.11.003.

[6] Zhao YZ, Zhai XM, Wang JH. Buckling behaviors and ultimate strengths of 6082-T6 aluminum alloy columns under eccentric compression–Part I: Experiments and finite element modeling. Thin-Walled Structures, 2019; 143: 106207. https://doi.org/10.1016/j.tws.2019.106207.

[7] Feng R, Mou XL, Chen ZM, et al. Finite-element modeling and design guidelines for axial compressive capacity of aluminium alloy circular hollow sections with holes. Thin-Walled Structures, 2020; 157: 107027. https://doi.org/10.1016/j.tws.2020.107027.

[8] Eurocode 9 (EC9): Design of aluminium structures. Part 1-1: General structural rules - General structural rules and rules for buildings. BS EN 1999-1-1:2007, European Committee for Standardization (CEN):2007. BSI; 2007.

[9] Baehre R. Trycktastravorav elastoplastikt material-nagrafragestallningar (Comparison between structural behaviour of elastoplastic material). Tekn Arne Johnson Ingenjorsbyra 1966. (in German)

[10] Wang YJ, Fan F, Lin SB. Experimental investigation on the stability of aluminium alloy 6082 circular tubes in axial compression. Thin-walled structures, 2015; 89: 54-66. https://doi.org/10.1016/j.tws.2014.11.017.

[11] Rong B, Guo Y, Li ZY. Study on the stability behavior of 7A04-T6 aluminum alloy square and rectangular hollow section columns under axial compression. Journal of Building Engineering, 2022; 45: 103652. https://doi.org/10.1016/j.jobe.2021.103652.

[12] Li BB, Wang YQ, Zhang Y, et al. Flexural buckling of high-strength aluminium alloy CHS columns. Structures. Elsevier, 2022; 43: 223-233. https://doi.org/10.1016/j.istruc.2022.06.036.

[13] Zhou F, Young B. Tests of concrete-filled aluminum stub columns. Thin-Walled Structures, 2008; 46(6): 573-

583. https://doi.org/10.1016/j.tws.2008.01.003.
[14] Zhou F, Young B. Concrete-filled aluminum circular hollow section column tests. Thin-Walled Structures, 2009; 47(11): 1272-1280. https://doi.org/10.1016/j.tws.2009.03.014.
[15] Zhou F, Young B. Numerical analysis and design of concrete-filled aluminum circular hollow section columns. Thin-walled structures, 2012; 50(1): 45-55. https://doi.org/10.1016/j.tws.2011.10.002.
[16] Zhou F, Young B. Concrete-filled double-skin aluminum circular hollow section stub columns. Thin-Walled Structures, 2018; 133: 141-152. https://doi.org/10.1016/j.tws.2018.09.037.
[17] Zhou F, Young B. Compressive strengths of concrete-filled double-skin (circular hollow section outer and square hollow section inner) aluminium tubular sections. Advances in Structural Engineering, 2019; 22(11): 2418-2434. https://doi.org/10.1177/1369433219842381.
[18] Zeng X, Wu WB, Huo JS, et al. The axial strength of concrete-filled aluminum alloy circular tubular stub columns. Engineering Mechanics, 2021; 38(02): 52-60. (In Chinese) DOI: 10.6052/j.issn.1000-4750.2020.03.0178.
[19] Zha XX, Gong YL. Behavior study of new-type concrete filled metal tubular (CFMT) columns I: Strength capacity of axially compressed short columns. Progress in Steel Building Structures. 2012; 14, 12–18. (In Chinese)
[20] Shi Y, Zhang JG, Wang T, et al. Experimental study on the axial compression performance of a new type of metal tube concrete short column. Building Structure, 2022; 52(3): 110-115 . (In Chinese) DOI: 0.19701 /j.jzjg. 20200291.
[21] Chen D, Qu H, Li W, et al. Mechanical property of seawater sea-sand concrete-filled aluminum alloy circular tubular columns under axial load. Journal of Yantai University (Natural Science and Engineering Edition), 2022; 35(04): 467-475. (In Chinese) DOI:10.13951/j.cnki.37-1213/n.211103.
[22] Wang FC, Zhao HY, Han LH. Analytical behavior of concrete-filled aluminum tubular stub columns under axial compression. Thin-Walled Structures, 2019; 140: 21-30. https://doi.org/10.1016/j.tws.2019.03.019.
[23] Ding FX, Liao CB, Wang E, et al. Numerical investigation of the composite action of axially compressed concrete-filled circular aluminum alloy tubular stub columns. Materials, 2021; 14(9): 2435. https://doi.org/ 10.3390/ma14092435.
[24] Patel VI, Liang QQ, Hadi MNS. Numerical simulations of circular high strength concrete-filled aluminum tubular short columns incorporating new concrete confinement model. Thin-Walled Structures, 2020; 147: 106492. https://doi.org/10.1016/j.tws.2019.106492.
[25] Yan XF, Ahmed M, He MN. Behavior and design of axially loaded high-strength concrete-filled circular aluminum tubular short columns. Structures. Elsevier, 2022; 44: 357-371. https://doi.org/10.1016/j.istruc. 2022.07.088.
[26] Zhang ZJ, Han FX, Liu Q. Experimental Study on Axial Compression Performance of 7A04 High Strength Aluminum Alloy Circular Tube Concrete Short Column. Geofluids, 2022. https://doi.org/10.1155/2022 /8270471.
[27] Deng ZH, Guo JH, Yu JJ, et al. Axial compression performance of coral concrete-filled aluminium tube (CCFAT) square stub columns. Case Studies in Construction Materials, 2021; 15: e00697. https://doi.org/ 10.1016/j.cscm.2021.e00697.
[28] Georgantzia E, Ali SB, Gkantou M, et al. Flexural buckling performance of concrete-filled aluminium alloy tubular columns. Engineering Structures, 2021; 242: 112546. https://doi.org/10.1016/j.engstruct.2021. 112546.
[29] Georgantzia E, Ali SB, Gkantou M, et al. Structural response of aluminium alloy concrete filled tubular columns. ce/papers, 2021; 4(2-4): 614-620. https://doi.org/10.1002/cepa.1339.
[30] Georgantzia E, Ali S.B, Gkantou M, et al. Numerical modelling of concrete-filled aluminium alloy 6082-T6 columns under axial compression. Journal of Physics: Conference Series. IOP Publishing, 2022; 2198(1): 012045. https://doi.org/10.1088/1742-6596/2198/1/012045
[31] Patel VI, Liang QQ, Hadi MNS. Numerical study of circular double-skin concrete-filled aluminum tubular stub columns. Engineering Structures, 2019; 197: 109418. https://doi.org/10.1016/j.engstruct.2019.109418.
[32] Zhao D, Zhang JG, Lu L, et al. The Strength in Axial Compression of Aluminum Alloy Tube Confined Concrete Columns with a Circular Hollow Section: Experimental Results. Buildings, 2022; 12(5): 699. https://doi.org/10.3390/buildings12050699.
[33] Ali SB, Kamaris GS, Gkantou M. Flexural buckling behaviour of concrete-filled double skin aluminium alloy columns. Engineering Structures, 2023; 275: 115316. https://doi.org/10.1016/j.engstruct.2022.115316
[34] Rong B, Zhang S, Zhang YC, et al. Study on the ultimate bearing capacity of 7A04-T6 CFAT columns under eccentric compression. Journal of Building Engineering, 2022; 46: 103654. https://doi.org/10.1016/j.jobe. 2021.103654.
[35] Ali SB, Kamaris GS, Gkantou M, et al. Numerical study of concrete-filled aluminium alloy tubular columns under eccentric compression. IOP Conference Series: Materials Science and Engineering. IOP Publishing, 2021; 1058(1): 012010. https://iopscience.iop.org/article/10.1088/1757-899X/1058/1/012010.

[36] Su MN, Young B, Gardner L. The continuous strength method for the design of aluminium alloy structural elements. Engineering Structures, 2016; 122: 338-348. https://doi.org/10.1016/j.engstruct.2016.04.040.
[37] Hill H.N. Determination of stress-strain relations from" offset" yield strength values. Aluminum Co of America Pittsburgh Pa, 1944.
[38] Gardner L, Ashraf M. Structural design for non-linear metallic materials. Engineering Structures, 2006; 28(6): 926-934. https://doi.org/10.1016/j.engstruct.2005.11.001.
[39] Abdella K. Inversion of a full-range stress–strain relation for stainless steel alloys. International Journal of Non-Linear Mechanics, 2006; 41(3): 456-463. https://doi.org/10.1016/j.ijnonlinmec.2005.10.002.
[40] Han LH, Yao GH, Tao Z. Performance of concrete-filled thin-walled steel tubes under pure torsion. Thin-Walled Structures, 2007; 45: 24–36. https://doi.org/10.1016/j.tws.2007.01.008.
[41] Steinhardt O. Aluminum constructions in civil engineering. Aluminum, 1971; 47: 131-139.
[42] Wang YJ, Fan F, Qian HL, et al. Experimental study on constitutive model of high-strength aluminum alloy 6082-T6. Journal of Building Structures, 2013; 34(06): 113-120. (In Chinese) DOI: 0.14006/j.jzjgxb. 2013.06.016.
[43] GB/T 228.1−2010, Metallic materials-tensile testing-Part 1: Method of test at room temperature. Beijing: Standards Press of China, 2011. (in Chinese)
[44] GB 50010-2015, Code for Design of Concrete Structures (GB 50010-2015), Ministry of Housing and Urban-Rural Development of the People's Republic of China, Beijing, China, 2015. (in Chinese)
[45] Goode CD, Lam D. Concrete-filled steel tube columns-tests compared with Eurocode 4. Composite Construction in Steel and Concrete VI. 2011; 317-325. https://doi.org/10.1061/41142(396)26.
[46] Wang FC, Han LH, Li W. Analytical behavior of CFDST stub columns with external stainless steel tubes under axial compression. Thin-Walled Structures, 2018; 127: 756-768. https://doi.org/10.1016/j.tws.2018. 02.021.
[47] GB 50396-2014. Technical code for concrete-filled steel tubular structures. Beijing: China Architecture & Building Press; 2014. (in Chinese)